



**Synthesis and SERS Application of Gold and Iron Oxide
Functionalized Bacterial Cellulose Nanocrystals
(Au@Fe₃O₄@BCNCs)**

Journal:	<i>Analyst</i>
Manuscript ID	AN-ART-04-2020-000711.R1
Article Type:	Paper
Date Submitted by the Author:	21-May-2020
Complete List of Authors:	Kang, Seju; Virginia Tech, Civil and Environmental Engineering Rahman, Asifur; Virginia Tech, Civil and Environmental Engineering Boeding, Ethan; Virginia Tech, Civil and Environmental Engineering Vikesland, Peter; Virginia Polytechnic Institute and State University, Civil and Environmental Engineering

1
2
3
4 **Synthesis and SERS Application of Gold and Iron Oxide**
5 **Functionalized Bacterial Cellulose Nanocrystals**
6 **(Au@Fe₃O₄@BCNCs)**
7
8

9 Seju Kang,^{a,b,1} Asifur Rahman,^{a,b,1} Ethan Boeding,^{a,b} Peter J. Vikesland,^{a,b*}
10

11 ^aDepartment of Civil and Environmental Engineering, Virginia Tech, Blacksburg, Virginia;
12

13 ^bVirginia Tech Institute of Critical Technology and Applied Science (ICTAS) Sustainable
14 Nanotechnology Center (VTSuN), Blacksburg, Virginia;
15
16
17
18

19 ¹These authors made equal contributions to this work.
20

21 * Corresponding author: pvikes@vt.edu
22
23
24
25
26
27
28
29
30
31
32
33
34
35
36
37
38
39
40
41
42
43
44
45
46
47
48
49
50
51
52
53
54
55
56
57
58
59
60

Abstract

Bacterial cellulose nanocrystals (BCNCs) are biocompatible cellulose nanomaterials that can host guest nanoparticles to form hybrid nanocomposites with a wide range of applications. Herein, we report the synthesis of a hybrid nanocomposite that consists of plasmonic gold nanoparticles (AuNPs) and superparamagnetic iron oxide (Fe_3O_4) nanoparticles supported on BCNCs. As a proof of concept, the hybrid nanocomposites were employed to isolate and detect malachite green isothiocyanate (MGITC) via magnetic separation and surface-enhanced Raman scattering (SERS). Different initial gold precursor (Au^{3+}) concentrations altered the size and morphology of the AuNPs formed on the nanocomposites. The use of 5 and 10 mM Au^{3+} led to a heterogenous mix of spherical and nanoplate AuNPs with increased SERS enhancements, as compared to the more uniform AuNPs formed using 1 mM Au^{3+} . Rapid and sensitive detection of MGITC at concentrations as low as 10^{-10} M was achieved. The SERS intensity of the normalized Raman peak at 1175 cm^{-1} exhibited a log-linear relationship for MGITC concentrations between 2×10^{-10} and 2×10^{-5} M for $\text{Au}@\text{Fe}_3\text{O}_4@\text{BCNCs}$. These results suggest the potential of these hybrid nanocomposites for application in a broad range of analyte detection strategies.

Introduction

Bacterial cellulose (BC) is a cellulose nanomaterial synthesized by a number of bacterial species (i.e., *Achromobacter*, *Alcaligenes*, and *Gluconacetobacter xylinus*) in liquid culture media.¹⁻³ Due to its facile synthesis and biocompatibility, BC has great potential for environmental, biomedical, and drug delivery applications.⁴⁻⁷ Hydroxyl groups on the BC surface enable attachment of diverse types of nanoparticles and production of BC-based nanocomposites. BC substrates can be functionalized with iron oxide (Fe_3O_4) nanoparticles due to their high reactivity

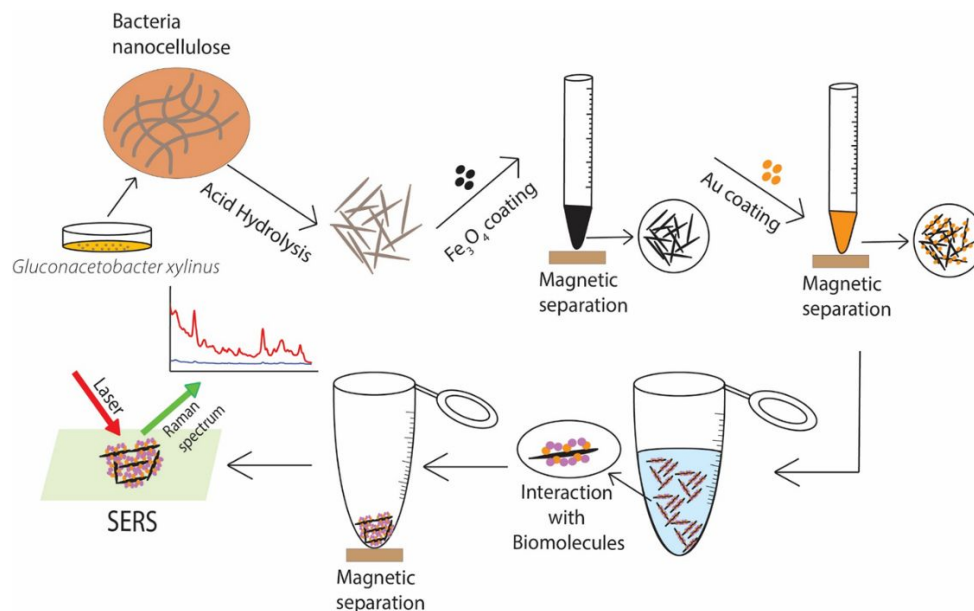
1
2
3 and capacity for magnetic separation.⁸⁻¹⁰ The facile synthesis and surface functionalization of BC
4 with Fe₃O₄ nanoparticles enables catalytic, biomedical, drug delivery and magnetic resonance
5 imaging (MRI) applications.^{11, 12} In addition, gold nanoparticle (AuNP) functionalized BCs have
6 potential applications as biosensors. AuNPs can be synthesized and deposited onto BC substrates
7 for analyte detection.^{3, 13} Adjacent plasmonic metal nanoparticles with nano-sized gaps enhance
8 inelastic Raman scattering signals due to the localized surface plasmon resonance effect – this
9 phenomenon makes surface-enhanced Raman spectroscopy (SERS) possible.^{14, 15} The high Raman
10 enhancement factors (10⁴ to 10¹²) of SERS makes it a promising technique for highly sensitive
11 detection (<ng L⁻¹).^{16, 17} The development of SERS substrates to optimize the Raman signal is a
12 highly interesting and active research area. Colloidal nanoparticles immobilized on cellulose
13 substrates are of growing interest because of the cost-effective preparation and scalability of the
14 approach.^{3, 18, 19}

15
16
17
18
19
20
21
22
23
24
25
26
27
28
29
30
31 Following strong acid hydrolysis of BC, bulk cellulose can be converted into highly
32 crystalline cellulose fragments commonly referred to as bacterial cellulose nanocrystals
33 (BCNCs).²⁰ The use of BCNCs is advantageous due to their high specific surface area, colloidal
34 and thermal stability, high tensile strength, and nanometric dispersity.^{2, 21, 22} In a recent study,
35 cationic BCNCs coated by amines and amine-containing polymers were developed as nucleic acid
36 nanocarriers.²³ Recently researchers developed hydroxypropyl methylcellulose combined with
37 BCNCs and silver nanoparticles to improve the tensile strength of a product potentially useful to
38 the food packaging industry.²⁴

39
40
41
42
43
44
45
46
47
48
49 In this study, we report the facile synthesis of hybrid BCNC-based nanocomposites coated
50 with AuNPs and Fe₃O₄ nanoparticles (Au@Fe₃O₄@BCNCs). Fe₃O₄ nanoparticles were
51 synthesized from an iron precursor dissolved in BCNC suspension and immobilized *in situ* onto
52
53
54
55
56
57
58
59
60

1
2
3 the BCNCs to form Fe_3O_4 nanoparticle coated BCNCs ($\text{Fe}_3\text{O}_4@\text{BCNCs}$). This step was followed
4
5 by the *in situ* reduction of Au^{3+} in the presence of $\text{Fe}_3\text{O}_4@\text{BCNCs}$ to produce $\text{Au}@\text{Fe}_3\text{O}_4@\text{BCNCs}$.
6
7 Previously, Au and Fe_3O_4 nanoparticles were combined in Au shell- Fe_3O_4 core materials and Au-
8
9 Fe heterodimers for application in target molecule binding and detection through optical SERS
10
11 sensing.^{25, 26} The production of core-shell nanoparticles exhibits many challenges such as the poor
12
13 diffusion barrier of the core layer due to shell formation, difficulties in controlling the uniformity
14
15 and thickness of the shell coating, and atomic lattice mismatches between the core and shell
16
17 components.^{25, 27, 28} BCNCs can potentially be used as alternative substrates that can readily bind
18
19 to guest metals such as Au and Fe_3O_4 nanoparticles through C=O-metal binding or electrostatic
20
21 interactions.^{4, 21} $\text{Fe}_3\text{O}_4@\text{BCNCs}$ can be quickly separated from suspension and can be used to
22
23 concentrate target molecules using an external magnetic field. Furthermore, Fe_3O_4 nanoparticles
24
25 can be easily detached from BCNCs following strong acid treatment and the BCNCs can then be
26
27 re-functionalized, making them environmentally friendly. The $\text{Fe}_3\text{O}_4@\text{BCNCs}$ can be further
28
29 functionalized with AuNPs to utilize the biocompatibility and plasmonic nature of AuNPs. The
30
31 $\text{Au}@\text{Fe}_3\text{O}_4@\text{BCNC}$ platform combines the magnetic separation capability of Fe_3O_4 nanoparticles
32
33 and SERS-active AuNPs for interaction with and SERS detection of organic molecules (**Scheme**
34
35 **1**).
36
37
38
39
40
41
42

43 The hybrid BCNC-based nanocomposites developed in this study were comprehensively
44
45 characterized using transmission electron microscopy (TEM), scanning electron microscopy (SEM)
46
47 and electrophoretic mobility measurements. As a proof-of-concept, we investigated the efficacy
48
49 of the nanocomposites for the detection of malachite green isothiocyanate (MGITC) by SERS with
50
51 different initial concentrations of Au^{3+} for functionalization.
52
53
54
55
56
57
58
59
60



Scheme 1. Schematic illustration of synthesis, functionalization, and SERS application of the Au@Fe₃O₄@BCNCs

Materials and Methods

Materials

Gold chloride trihydrate (HAuCl₄·3H₂O, ≥99.9%), sodium citrate tribasic dihydrate (Na₃Cit·2H₂O, ≥99.0%), fructose, yeast extract, calcium carbonate (CaCO₃, Reagent Plus), ammonium hydroxide (NH₃OH, ACS Reagent, 28-30% NH₃ basis), and iron(II) chloride (98%) were obtained from Sigma-Aldrich (St. Louis, MO, USA). Sodium hydroxide (NaOH, certified ACS), hydrochloric acid (HCl, certified ACS plus), ferric chloride hexahydrate (FeCl₃·6H₂O, certified ACS) and malachite green isothiocyanate (MGITC) were purchased from Thermo Fisher Scientific (Hampton, NH, USA). Deionized (DI) water was ultrapure with ≥ 18 MΩ cm resistance.

Synthesis of BC pellicles followed by BCNC preparation

BC pellicles in petri dishes were synthesized following a published approach with minor revision.³ The cellulose-producing bacterial strain *Gluconacetobacter xylinus* (*G. xylinus*) was used to produce the BC pellicles. Prior to inoculating with *G. xylinus*, all media was autoclaved at 121 °C and 15 psi for 20 mins. Approximately 10 mL aliquots of ATCC medium 459 (10 g fructose, 1 g yeast extract, and 2.5 g CaCO₃ in 200 mL of DI water) were poured into 100 mm diameter, 15 mm deep petri dishes. One or two visible *G. xylinus* colonies that had formed on nutrient agar were scooped and inoculated into each ATCC medium. This inoculated medium was quiescently stored in a 303 K oven for five days. After five days of incubation, hydrogel-like BC pellicles were generated. These pellicles were removed and rinsed using tap water to remove residual bacterial cells and nutrients. Following this cleaning, the BC pellicles were immersed in 0.1 M NaOH and stirred for three days to remove remaining residuals and hinder additional cellulose production. The cleaned BC pellicles were stored in DI water at room temperature until use.

To prepare a BCNC suspension, a single piece of BC pellicle was hydrolyzed with 10-15 mL of 37 % (w/w) HCl solution at 80°C for 3.5 hours under continuous stirring. The acid hydrolysis reaction was then terminated and 40 mL of DI water was added to the reaction flask. The resulting cloudy and acidic BCNC suspension was centrifuged at 4,000 rpm for 30 mins. After centrifugation, the sediment was collected and re-suspended in DI water. This cycle was repeated until the pH of the BCNC suspension was between 6-7.

Functionalization with Fe₃O₄ nanoparticles and AuNPs

The BCNCs were centrifuged and mixed in 20 mL of DI water containing FeCl₃·6H₂O and FeCl₂ in a 2:1 molar ratio. The mixture was transferred to a round bottom flask and was purged with N₂ gas for 1 hour while being magnetically stirred at 600 rpm. The suspension was then heated

1
2
3 to 80 °C in a silicone oil bath and 5 mL of NH₄OH (28-30%) was added dropwise using a syringe.
4
5 Upon addition of NH₄OH, the color of the suspension changed from orange/yellow to black, which
6
7 indicated the attachment of Fe₃O₄ nanoparticles onto the BCNCs. The suspension was stirred for
8
9 30 mins and then cooled to room temperature. The cooled suspension was diluted to 50 mL in DI
10
11 water and was repeatedly washed and magnetically separated until excess Fe₃O₄ nanoparticles
12
13 were fully removed. These magnetic separations were performed using a neodymium disc magnet
14
15 (N52, 40×20 mm). Finally, the Fe₃O₄@BCNCs were stored in 50 mL of DI water.
16
17
18

19 To functionalize Fe₃O₄@BCNCs with AuNPs, 5 mL aliquots of Fe₃O₄@BCNC suspension
20
21 were transferred into a conical tube. A magnetic field was applied to separate the nanocomposites.
22
23 The supernatant was decanted and replaced with a fixed 5 mL volume of either 1, 5, or 10 mM
24
25 HAuCl₄. To accelerate the reduction of Au³⁺ to AuNPs, Na₃Cit was added as a reducing agent. For
26
27 each HAuCl₄ concentration, small aliquots of Na₃Cit (~ 200 μL) were added into the samples at a
28
29 1:1 molar ratio of HAuCl₄ and Na₃Cit. The samples were then incubated at 303 K overnight. The
30
31 yellow Au³⁺ suspension rapidly changed to brown indicating the reduction of Au³⁺ to AuNP. The
32
33 samples were repeatedly washed with DI water by magnetic separation and re-suspension until the
34
35 supernatant became transparent indicating the removal of non-deposited AuNPs.
36
37
38

39 **Characterization of the Au@Fe₃O₄@BCNCs**

40
41
42 TEM was used to observe the morphology of the BCNCs, Fe₃O₄@BCNCs, and
43
44 Au@Fe₃O₄@BCNCs. The as-synthesized BCNC suspension [(~ 0.01% (w/v))] was deposited on a
45
46 carbon mesh 200 grid (Ted Pella, Inc; Redding, CA), dried, and negatively stained with 2% uranyl
47
48 acetate solution. The Fe₃O₄@BCNCs and Au@Fe₃O₄@BCNCs were diluted 10× and 10 μL of
49
50 each sample was deposited onto the TEM grid without staining because negative staining can
51
52 affect the imaging of Au and Fe₃O₄. TEM analysis was conducted using a field emission gun
53
54
55
56
57
58
59
60

1
2
3 instrument (JEOL 2100) operating at an accelerating voltage of 200 kV. Nanoparticle sizes in each
4
5 sample were determined (n=50) using ImageJ software. The morphologies of AuNPs on the
6
7 Au@Fe₃O₄@BCNCs were characterized using a field-emission Quanta 600 FEG environmental
8
9 SEM. Secondary electron (InLens detector) mode was used to obtain contrast between aggregated
10
11 BCNCs and AuNPs, while backscattered electron (RBSD detector) mode was used for energy
12
13 dispersive spectroscopy (EDS) mapping and analysis. To compare the surface charge and stability
14
15 of the different nanocomposites, electrophoretic mobility (U_E , m^2Vs^{-1}) was measured using a
16
17 Zetasizer Nano DLS (Malvern Nano ZS, Malvern, UK). U_E indicates particle response to an
18
19 applied electric field and is measured by doppler frequency shifts in scattered light.
20
21
22
23

24 **Proof-of-concept SERS application of the Au@Fe₃O₄@BCNCs**

25
26 For the detection experiment, MGITC was selected because it has a large Raman cross-
27
28 section and high affinity to the AuNP surface due to its thiol group.^{29, 30} In a 2-mL tube, different
29
30 concentrations of 500 μ L MGITC solution were added into 500 μ L of Au@Fe₃O₄@BCNC
31
32 suspension. Following 3-4 hours of incubation at room temperature, the nanocomposites were
33
34 magnetically separated and the supernatant was decanted. A preliminary test of sorption kinetics
35
36 for MGITC was conducted by using the UV-Vis spectrophotometer. This test indicated that
37
38 sorption reached equilibrium approximately within 2 hours (**Figure S1**). The residue was re-
39
40 suspended using 10 μ L of DI water and pipetted onto a glass slide. Raman spectra were collected
41
42 using a WITec alpha500R Raman spectrometer (WITec GmbH, Ulm, Germany, spectral
43
44 resolution = ~ 3.5 cm^{-1}), with a 785-nm laser (5 mW intensity) and a 10 \times confocal microscope
45
46 objective. The signal was collected using a Peltier cooled charge-coupled device (CCD) with 300
47
48 grooves per mm grating set. For each sample, a total of 20 \times 20 points (X \times Y) were acquired across
49
50 a 10 \times 10 μm^2 area with 0.1 s integration time for each point.
51
52
53
54
55
56
57
58
59
60

SERS data analysis

For the collected Raman spectra, the baselines were corrected using an asymmetric least square smoothing method coded through Mathworks MATLAB/SIMULINK software (ver. R2019b). After baseline correction, the Raman intensities of the peaks of interest at 1175 and 77 cm^{-1} (I_{1175} and I_{77}) were extracted and the intensity ratio of the peaks (I_{1175}/I_{77}) was plotted against the logarithm of MGITC concentrations.

To calculate the limit of detection (LOD) of the Au@Fe₃O₄@BCNCs, the best-fit regression line was determined as follows,

$$I_{1175}/I_{77} = \hat{a} \log C + \hat{b}$$

where \hat{a} and \hat{b} are the slope and y intercept of the regression line. The LOD was calculated using the following the equation,

$$\log \text{LOD} = (3\sigma_{\hat{a}} - \hat{b}) / \hat{a}$$

$\sigma_{\hat{a}}$ is the standard deviation of the slope of the regression line.

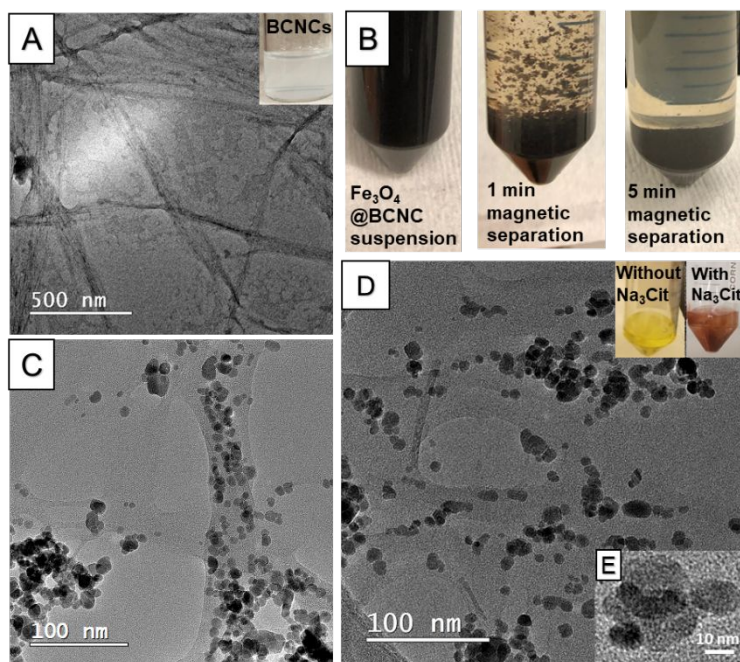
Results and Discussion

Synthesis and characterization of the nanocomposites

TEM images of the as-synthesized BCNCs revealed rod or needle shaped structures 30-40 nm in width and 400-800 nm in length (**Figure 1A**). We did not perform post-treatment steps such as dialysis or filtration on the BCNC samples and this explains the presence of some impurities in the sample. The morphologies of the HCl-hydrolyzed BCNCs in this study are similar to those reported previously by Singhsa et. al.²³ HCl-hydrolysis has been reported to produce cellulose nanocrystals (CNCs) in greater yield and larger dimensions relative to H₂SO₄-hydrolysis.^{23, 31}

Given that the charged SO_4^{2-} groups from H_2SO_4 can compromise the thermostability of the nanocrystals, HCl is thought to better optimize the CNC hydrolysis conditions.^{31,32}

The $\text{Fe}_3\text{O}_4@$ BCNCs were prepared by the *in situ* synthesis of Fe_3O_4 nanoparticles on the BCNCs. Upon attachment of Fe_3O_4 nanoparticles, the Fe precursor/BCNC solution turned black indicating the formation of Fe_3O_4 nanoparticles. Following synthesis, the $\text{Fe}_3\text{O}_4@$ BCNCs could be completely separated from suspension within 5 mins using a magnetic field (40×20 mm N52 neodymium disc magnet) (**Figure 1B**). AuNP functionalization of $\text{Fe}_3\text{O}_4@$ BCNCs was done by the *in situ* reduction of Au^{3+} using Na_3Cit as reducing agent. Na_3Cit is a widely used reducing agent that accelerates AuNP formation.^{3, 33} Upon AuNP formation, the color of the $\text{Au}@$ $\text{Fe}_3\text{O}_4@$ BCNC suspension changed from black to dark brown suggesting a higher reduction capacity of Na_3Cit compared to the BCNC-OH surface functional groups as reported previously (**Figure 1D**).³

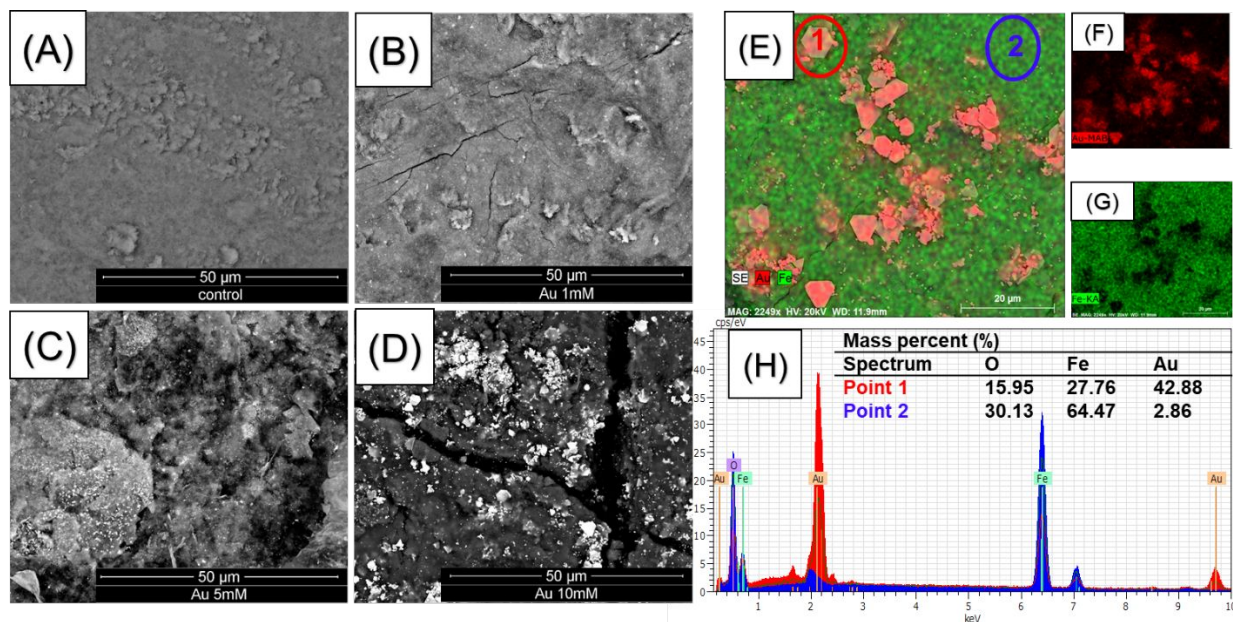


1
2
3 **Figure 1.** (A) TEM image of as-synthesized BCNCs (B) Fe₃O₄ coated BCNCs in suspension and
4 magnetically separated (C) TEM image of Fe₃O₄@BCNCs, (D) TEM image of
5 Au@Fe₃O₄@BCNCs and (E) Au and Fe₃O₄ nanoparticles.
6
7
8
9

10 FT-IR analysis of the BCNCs, BCNCs with Fe precursor, Fe₃O₄@BCNCs and
11 Au@Fe₃O₄@BCNCs were performed to analyze the nature of the chemical bonding of BCNCs
12 with nanoparticles. In the presence of Fe precursors and after Fe₃O₄ nanoparticle formation via Fe
13 reduction, the peak at around 3340 cm⁻¹ (BCNC-OH group) did not show any major shift (**Figure**
14 **S2A**). This result suggests limited Fe-OH binding to the BCNC surface and an apparent
15 electrostatic interaction between the -OH and Fe⁺³ seems to govern the interactions between
16 BCNC-OH and Fe₃O₄ nanoparticles.^{21, 34, 35} FT-IR spectra of the Au@Fe₃O₄@BCNCs had similar
17 peaks to the uncoated BCNC sample. All samples had characteristic FT-IR peaks at 3345 cm⁻¹, the
18 O-H stretching vibration, and at 1640 cm⁻¹, attributed to -OH groups of adsorbed water (**Figure**
19 **S2**).^{21, 36} Other identified peaks were at 2896 cm⁻¹ (C-H stretching) and 1060-1162 cm⁻¹ (C-O and
20 C-O-C stretching bonds in BCNC), suggesting no significant degradation of the BCNCs during
21 Au and Fe₃O₄ functionalization (**Figure S2**).
22
23
24
25
26
27
28
29
30
31
32
33
34
35
36
37
38

39 The morphologies of the nanoparticles within the Fe₃O₄@BCNCs and the
40 Au@Fe₃O₄@BCNCs were characterized using TEM. **Figures 1C** and **1D** show the typical
41 morphology of the Fe₃O₄@BCNCs and the 5 mM Au@Fe₃O₄@BCNCs nanocomposites, with Au
42 typically showing higher contrast (**Figure 1E**). The as-synthesized BCNCs were stained with 2%
43 uranyl acetate before TEM imaging and hence showed higher contrast (**Figure 1A**) compared to
44 the unstained Au and Fe₃O₄ functionalized BCNCs (**Figures 1C, 1D**). The average nanoparticle
45 diameter in the Fe₃O₄@BCNC samples was 9.43 ± 3.45 nm (n=50). After treatment with 5 mM
46 Au³⁺, the average nanoparticle size increased to 11.75 ± 2.4 nm (n=50). To better differentiate
47
48
49
50
51
52
53
54
55
56
57
58
59
60

1
2
3 between the Au and Fe₃O₄ nanoparticles, we performed backscattered electron imaging and EDS
4 analysis on magnetically separated and aggregated BCNC samples. As shown in **Figure 2 (A to**
5
6
7
8 **D)**, backscattered SEM images revealed an increased presence of Au on the aggregated
9 Fe₃O₄@BCNC surface with an increase in initial Au precursor loading. An increase in the initial
10 Au³⁺ concentration, from 1 to 5 mM caused formation of increased numbers of dispersed AuNPs.
11 A further increase in Au³⁺ concentration to 10 mM caused the scattered formation of aggregated
12 AuNPs and Au nanoplates. Previously, Wei et. al. observed Au nanoplate formation in AuNP
13 coated BC substrates with Au³⁺ concentrations of 10 mM or higher.³ In addition, EDS mapping of
14 the aggregated 10 mM Au@Fe₃O₄@BCNC sample (**Figure 2, E-G**) suggested plate-like AuNPs.
15 EDS spectra (**Figure 2H**) of an AuNP nanoplate (**Figure 2E**, point 1) showed a higher mass
16 percent (42.88%) of Au compared to Au (2.86 mass %) directly associated with Fe₃O₄
17 nanoparticles (**Figure 2E**, point 2).



1
2
3 **Figure 2.** Backscattered SEM images of the aggregated (A) $\text{Fe}_3\text{O}_4@\text{BCNCs}$, (B) 1 mM
4 $\text{Au}@\text{Fe}_3\text{O}_4@\text{BCNCs}$, (C) 5 mM $\text{Au}@\text{Fe}_3\text{O}_4@\text{BCNCs}$ and (D) 10 mM $\text{Au}@\text{Fe}_3\text{O}_4@\text{BCNCs}$. EDS
5
6 mapping of (E) 10mM $\text{Au}@\text{Fe}_3\text{O}_4@\text{BCNCs}$ with (F) Au and (G) Fe elements highlighted. The
7
8 corresponding (H) EDS spectra of the map are provided with mass percent of O, Fe, and Au shown.
9
10
11
12
13
14
15

16 Magnetic separation of the $\text{Au}@\text{Fe}_3\text{O}_4@\text{BCNCs}$ in suspension induces nanocomposite
17 aggregation, which can potentially form aggregated structures (**Figure 2E**). Aggregated AuNPs
18 and Au nanoplates are typically characterized by strong SERS enhancements.^{3, 37, 38} Magnet
19 induced aggregation has been used previously for core-shell $\text{Au}@\text{Fe}_3\text{O}_4$ nanoparticles to produce
20 interparticle “hot-spots” that can amplify the Raman signals to achieve highly-sensitive
21 detection.²⁶
22
23
24
25
26
27
28
29

30 The effect of surface functionalization by Au and Fe_3O_4 on the electrophoretic mobility of
31 the BCNCs is shown in **Figure 3**. The pH_{IEP} of the samples was estimated based upon where the
32 electrophoretic mobility goes to zero as a function of solution pH in 0.01 M NaCl suspensions.
33 HCl-hydrolyzed BCNCs exhibited a strongly negative surface potential and were stable in NaCl
34 suspension. At higher electrolyte (NaCl) concentrations of 0.025M or more, CNCs are reported to
35 aggregate with a concomitant increase in hydrodynamic diameter.³⁹ Upon functionalizing with
36 Fe_3O_4 nanoparticles, the electrophoretic mobility for the $\text{Fe}_3\text{O}_4@\text{BCNCs}$ was similar to that of
37 bare Fe_3O_4 nanoparticles. This result contrasts with the unfunctionalized BCNCs, which showed
38 mostly negative surface charge between pH 2 to 10. The pH_{IEP} of the $\text{Fe}_3\text{O}_4@\text{BCNCs}$ was
39 estimated to be 5.9, similar to bare Fe_3O_4 nanoparticles. After functionalizing with 1 and 10 mM
40 Au^{3+} , the pH_{IEP} of the nanocomposites shifted to between pH 3 and 4. Upon AuNP formation, the
41 $\text{Au}@\text{Fe}_3\text{O}_4@\text{BCNCs}$ showed negative surface charge at or above pH 4, similar to the observations
42
43
44
45
46
47
48
49
50
51
52
53
54
55
56
57
58
59
60

in previous studies for Au nanoshell bearing cellulose nanocrystals and AuNPs.^{40, 41} Attachment of Au and Fe₃O₄ nanoparticles onto the BCNCs was carefully controlled to utilize the efficiency of both the magnetic and plasmonic properties of the hybrid nanocomposites. The electrophoretic mobility measurements suggest that using the stated amount of Fe and Au precursors, the resulting nanocomposites showed charge stability in suspension and minimal aggregation at a low salt concentration of 0.01 M NaCl.

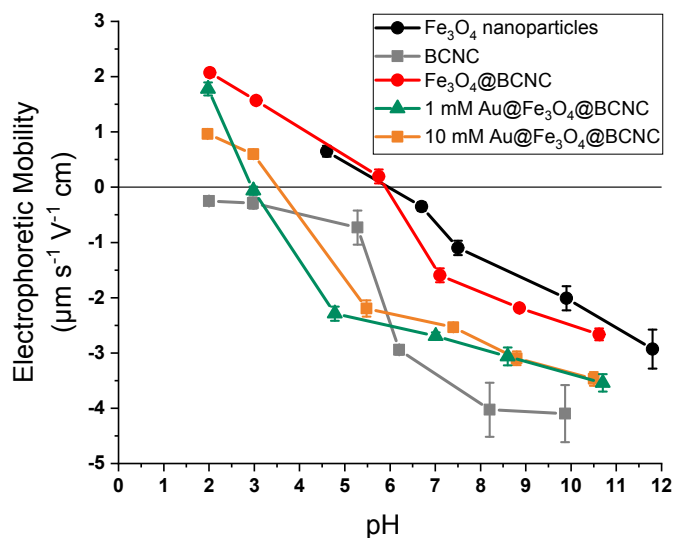


Figure 3. Electrophoretic mobility of bare Fe₃O₄ nanoparticles, BCNCs, Fe₃O₄@BCNCs, 1 mM and 10 mM Au@Fe₃O₄@BCNCs in 0.01 M NaCl solution. The error bars indicate standard deviation of three measurements.

SERS detection of MGITC using the nanocomposites

Using the Au@Fe₃O₄@BCNCs, SERS detection of MGITC was rapid and sensitive. Following sorption of MGITC to the nanocomposites, we readily separated the MGITC-sorbed nanocomposites from the suspension using a magnetic field. Within a few minutes, the suspension became transparent and the nanocomposites were concentrated near the magnet. Once the

transparent supernatant was decanted, the nanocomposites were re-dispersed in 10 μL of DI water. After deposition of 10 μL of the droplet including the MGITC-sorbed nanocomposite onto the glass slide, we successfully collected the SERS spectra with several distinct peaks under both dry and wet conditions (**Figure 4A**). The occurrence of a peak at 215 cm^{-1} corresponding to the Au–S bond demonstrates the successful complexation of isothiocyanate ($-\text{N} = \text{C} = \text{S}$) in MGITC to the AuNP surface.³⁰ The most prominent peaks at 1175 , 1366 , and 1589 cm^{-1} can be assigned to the n-plane benzene ν_9 mode, the aromatic ring stretching mode, and the in-plane aromatic ring stretching/bending mode, respectively.^{42, 43} Other distinct peaks such as 914 , 1296 , and 1618 cm^{-1} arise from the B_{1u} in-plane benzene ring mode, in-plane C–H or C–C–H bending mode, and phenyl-N stretching mode.^{42, 43}

In **Figure 4A**, insets show the pictures of the $\text{Au}@Fe_3O_4@BCNCs$ in the dry and wet states. The coefficients of variance (CV) of the SERS band at 1175 cm^{-1} across the scanning area in both states were 13.8 and 14.0%, respectively (**Figure S3**). This result demonstrates that both conditions had low spatial variability. For the dry sample, it was quickly dried within ~ 5 mins in the oven at $60\text{ }^\circ\text{C}$. The collection time of the SERS spectra across a $10\text{ }\mu\text{m} \times 10\text{ }\mu\text{m}$ area for one sample is only 40 s for 400 points in this study. The short intervals among analyte contact, sample separation, and data collection illustrate the rapid detection of MGITC using the $\text{Au}@Fe_3O_4@BCNCs$.

The overall SERS signals in a dry state were ~ 20 times higher than in the wet state (**Figure 4A**). After the droplet was dried, the $\text{Au}@Fe_3O_4@BCNCs$ were densely packed at the edge due to the coffee ring effect and the distance between AuNPs became closer resulting in the formation of denser SERS hot-spots, especially at the edge. Additionally, we applied a magnetic field to the deposited droplet of the suspended MGITC-sorbed nanocomposites before drying to investigate if SERS intensities could be further enhanced (**Figure S4**). However, there was no significant effect

on SERS enhancement, implying that the concentrated nanocomposites via the initial magnetic separation from suspension predominantly affected generation of SERS hot-spots. Hereafter, all SERS spectra were collected in the dry state due to its higher SERS enhancement.

The effect of the initial concentration of Au^{3+} during the functionalization experiments on the SERS performance of $\text{Au}@Fe_3O_4@BCNC$ was investigated. **Figure 4B** shows the SERS spectra of 2 μM MGITC using $\text{Au}@Fe_3O_4@BCNC$ s with different Au coating concentrations (1, 5, and 10 mM). It was observed that the peak intensities corresponding to MGITC increased with an increase in the initial concentration of Au^{3+} . The SERS enhancement depends on the density, size, and morphology of AuNPs on the nanocomposite.³ The nanocrystals in our study provided more favorable SERS hot-spots with a higher initial concentration of Au^{3+} . This observation may be attributed to the relatively larger size and quantity of AuNPs and formation of Au nanoplates, as observed in the SEM analysis (**Figure 2E**). The heterogenous morphologies of plasmonic Au metals present on the BCNCs can potentially improve SERS enhancement.^{37, 38}

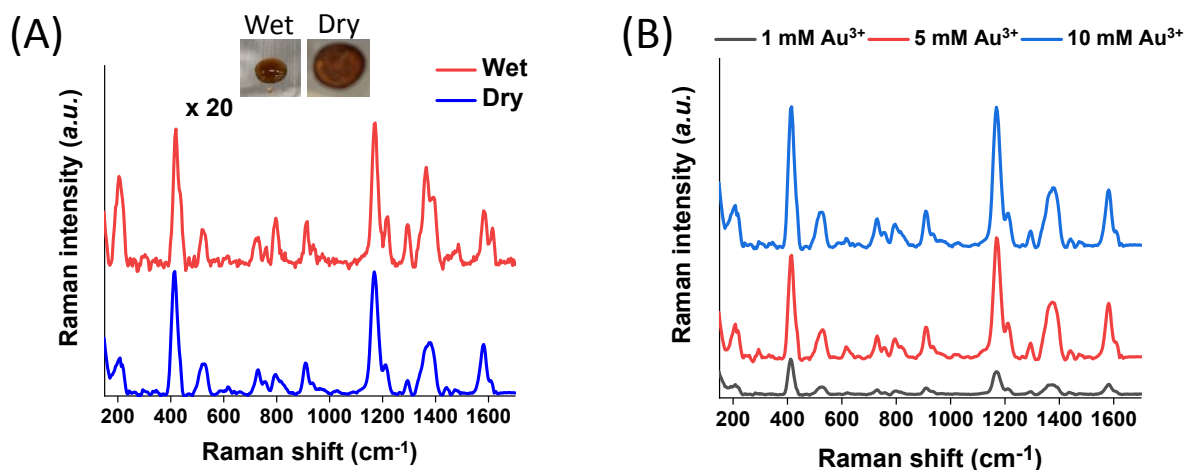


Figure 4. (A) Comparison of the SERS spectra of 2 μM MGITC under wet and dry conditions using 10 mM $\text{Au}@Fe_3O_4@BCNC$ s. Inset pictures show before/after drying of 10 μL of the droplet including the nanocomposites (B) The SERS spectra of 2 μM MGITC using the

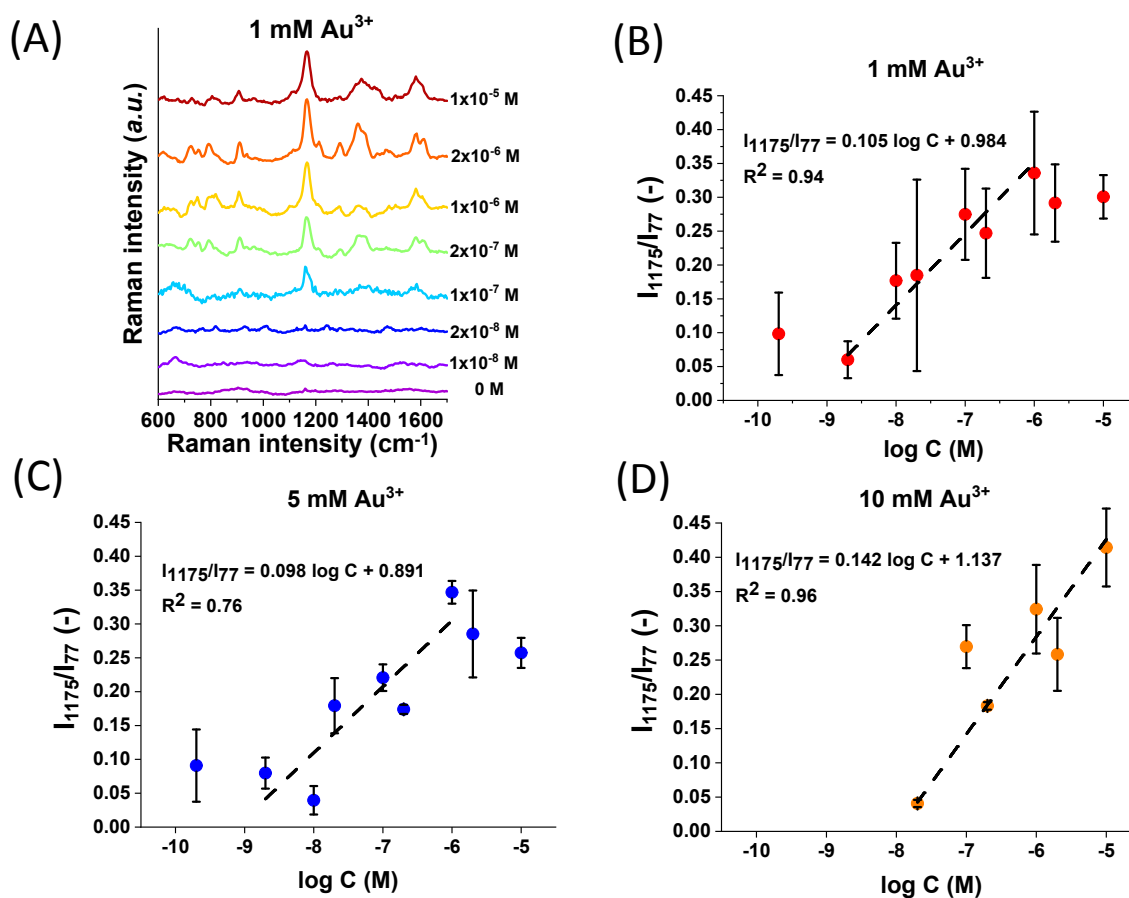
1
2
3 Au@Fe₃O₄@BCNCs with different Au coating condition (1, 5, and 10 mM Au³⁺). All spectra
4
5 shown here are the average of 400 collected spectra.
6
7

8 **Quantification of MGITC using SERS**

9

10 We successfully detected MGITC with concentrations ranging from 2×10^{-5} to 2×10^{-10} M
11 using the Au@Fe₃O₄@BCNCs. However, quantification was challenging due to the large variation
12 in the spatial arrangement of heterogenous SERS hot-spots among the batches arising from random
13 aggregation of the nanocomposites. Therefore, we normalized the SERS hot-spots between
14 different batches by using the intensity of the 77 cm⁻¹ pseudo-peak (I_{77}) as the internal standard.
15 As discussed previously, I_{77} reflects elastically scattered light from the amplified spontaneous
16 emission (ASE) of the Raman laser cut by the edge filter. In previous studies, it was reported that
17 the density of SERS hot-spots can be reflected by the variation of I_{77} .⁴⁴⁻⁴⁷ **Figure 5A** shows
18 vertically stacked SERS spectra of different concentrations of MGITC using 1 mM
19 Au@Fe₃O₄@BCNCs relative to a nanocomposite only control. All SERS spectra were averaged
20 from 400 individual spectra and normalized by I_{77} . It is noteworthy that the normalized intensities
21 of the peaks were higher for higher concentrations of MGITC. For quantification, among many
22 prominent peaks, the strongest peak at 1175 cm⁻¹ was selected as representative.^{48, 49} For each of
23 the 1, 5, and 10 mM Au³⁺ coating conditions, the normalized Raman intensities at 1175 cm⁻¹
24 (I_{1175}/I_{77}) were plotted against the logarithm of the MGITC concentration (**Figure 5B-D**). A linear
25 relationship between Raman intensity and the logarithm of analyte concentrations is commonly
26 observed in quantitative analysis of plasmonic nano-substrates.⁵⁰⁻⁵² We suggest that hot-spot
27 normalized Raman intensities further enhance quantification and account for the spatial
28 heterogeneity of AuNPs. These plots showed a clear linear trend between the two variables in a
29 certain range with R-squared values between 0.76 – 0.96. The lowest intensities of MGITC-
30
31
32
33
34
35
36
37
38
39
40
41
42
43
44
45
46
47
48
49
50
51
52
53
54
55
56
57
58
59
60

1
2
3 corresponding peaks were observed at $\sim 10^{-10}$ M for 1 and 5 mM Au@Fe₃O₄@BCNCs. On the
4
5 other hand, no distinct peaks were detected at $< 10^{-8}$ M for 10 mM Au@Fe₃O₄@BCNCs which
6
7 may be attributed to the decreased surface area of AuNP or Au nanoplate for MGITC sorption.
8
9 Surprisingly, the Au@Fe₃O₄@BCNCs at the lower initial concentration of Au³⁺ tended to have a
10
11 larger capacity for MGITC and ultimately higher detection sensitivity despite lower SERS
12
13 enhancement. The sorption capacity of the Au@Fe₃O₄@BCNCs for MGITC depends on the
14
15 surface area of Au regarding the strong Au-S bond between them. A higher fraction of AuNPs at
16
17 the lower initial concentration of Au³⁺ would provide a larger Au surface area, resulting in greater
18
19 sorption capacity for MGITC than plate-like Au at higher concentration.
20
21
22
23



1
2
3 **Figure 5.** SERS detection of MGITC using the Au@Fe₃O₄@BCNCs (A) The SERS spectra of
4 MGITC with the different concentrations using 1 mM Au@Fe₃O₄@BCNC stacked vertically for
5 clarity (B)-(D) The plots of the normalized peak of 1175 cm⁻¹ (I_{1175}/I_{77}) vs the logarithm of
6 concentrations of MGITC using 1, 5, and 10 mM Au@Fe₃O₄@BCNCs. Symbol and error bar
7 represent the average and standard deviation of 400 spectra for each point, respectively.
8
9
10
11
12
13
14
15
16
17

18 The linear regression between the normalized I_{1175} and the logarithm of the concentration
19 of MGITC was evaluated for all the Au@Fe₃O₄@BCNCs. The range of concentrations was
20 restricted to the range from 2×10^{-9} to 2×10^{-6} M and the data points with responses comparable to
21 the blank were omitted. The results shown in **Figure 6** suggest that the normalized I_{1175} can be
22 reasonably approximated as a linear function of the logarithm of the MGITC concentration. The
23 two parameters were statistically correlated with an R-square value of 0.79 and the experimental
24 data were within the 95% prediction region. Using this approach, the LOD was determined to be
25 5.8×10^{-10} M from the empirical best-fit equation (i.e., $I_{1175}/I_{77} = 0.837 + 0.087 \log C$) and the
26 standard error of the regression.⁵³ We expect that it will be possible to further lower the LOD value
27 by adjusting the size and morphology of AuNPs. Overall, this result demonstrates the applicability
28 of Au@Fe₃O₄@BCNCs for quantitative SERS analysis.
29
30
31
32
33
34
35
36
37
38
39
40
41
42
43

44 We believe that tuning the Au and Fe₃O₄ nanoparticles in the experiment can improve the
45 SERS performance of the Au@Fe₃O₄@BCNCs along with their magnetization capability in an
46 interactive manner. In a previous study, core-shell Au-coated Fe₃O₄ nanoparticles showed a
47 substantial reduction of the saturation magnetization compared to the bare Fe₃O₄ nanoparticles
48 which may be attributed to the shielding effect of the Au layer on the outer side of magnetite.⁵⁴
49 Further research on optimization of experimental functionalization conditions is required for these
50
51
52
53
54
55
56
57
58
59
60

hybrid nanocomposites to expand their applicability.

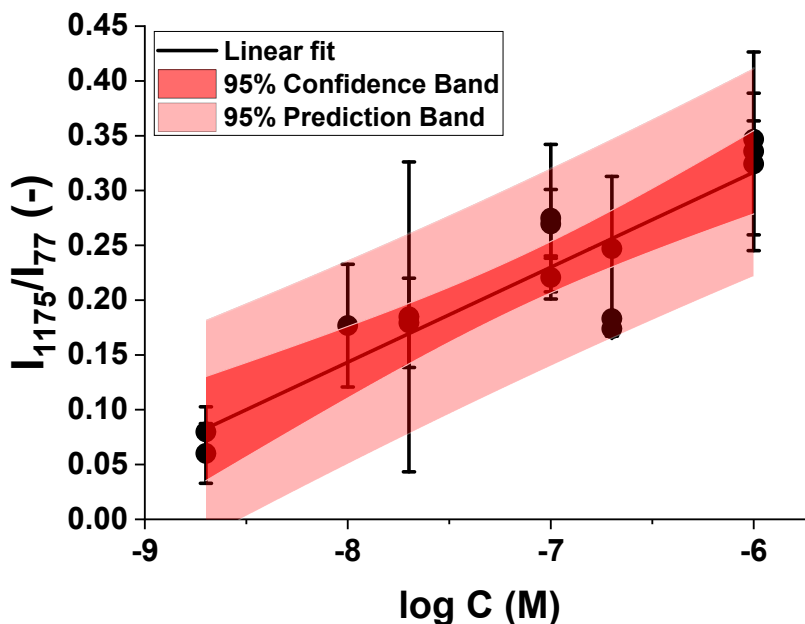


Figure 6. The comprehensive plot of the normalized Raman peak of 1175 cm^{-1} vs. the logarithm of the concentrations of MGITC using 1, 5, and 10 mM $\text{Au@Fe}_3\text{O}_4\text{@BCNCs}$. The black solid line shows the best-fit linear curve. Dark and light red-colored regions show statistical 95% confidence and prediction bands, respectively. $R^2 = 0.79$, Linear fit: $I_{1175}/I_{177} = 0.837 + 0.087 \log C$.

Conclusions

In this work, BCNCs were prepared by HCl hydrolysis of BC pellicles. The hybrid BC-based nanocomposites, $\text{Au@Fe}_3\text{O}_4\text{@BCNCs}$, were prepared by the sequential *in situ* synthesis of Fe_3O_4 and AuNPs in the presence of BCNCs. The efficacy of the hybrid nanocomposites as biomolecule binding and detection agents was evaluated through SERS detection of MGITC as a proof-of-concept. The structure of the BCNCs was unaffected after functionalizing with Fe_3O_4 and AuNPs. The size and morphology of AuNPs on the BCNCs were affected by the initial

1
2
3 concentration of Au^{3+} . The formation of heterogenous mixtures of aggregated AuNPs and Au
4 nanoplates at high Au^{3+} concentration could be responsible for high SERS intensity. Magnetic
5 separation-induced generation of SERS hot-spots from the aggregated $\text{Au}@Fe_3O_4@BCNCs$ had
6 low spatial variability under both wet and dry conditions. Different concentration levels of MGITC
7 were quantified through linear relationship between the normalized Raman peak of 1175 cm^{-1} vs.
8 the logarithmic concentrations of MGITC. These results suggest that the $\text{Au}@Fe_3O_4@BCNCs$
9 used in this study have great potential for biomolecular interaction and detection with high
10 sensitivity. Considering their facile synthesis procedure and biodegradability, the
11 $\text{Au}@Fe_3O_4@BCNCs$ can have a wide range of environmental and biological applications and
12 expected low environmental impacts.
13
14
15
16
17
18
19
20
21
22
23
24
25
26
27
28

29 **Acknowledgements**

30
31
32 Funding for this work was provided through US NSF grants CBET-1705653 and CBET-2029911
33 to P.V. Laboratory and instrumentation support was provided by NanoEarth a node of the NSF
34 supported NNCI (NSF award number #1542100). Additional support was provided by the
35 Sustainable Nanotechnology Interdisciplinary Graduate Program (VTSuN IGEP) funded by the
36 Virginia Tech Graduate School. Some icons in the graphical abstract were created with
37 BioRender.com.
38
39
40
41
42
43
44
45
46
47
48
49
50
51
52
53
54
55
56
57
58
59
60

References

1. Iguchi, M.; Yamanaka, S.; Budhiono, A., Bacterial cellulose—a masterpiece of nature's arts. *Journal of materials science* **2000**, *35*, (2), 261-270.
2. Thomas, B.; Raj, M. C.; Joy, J.; Moores, A.; Drisko, G. L.; Sanchez, C. m., Nanocellulose, a versatile green platform: from biosources to materials and their applications. *Chemical reviews* **2018**, *118*, (24), 11575-11625.
3. Wei, H.; Rodriguez, K.; Renneckar, S.; Leng, W.; Vikesland, P. J., Preparation and evaluation of nanocellulose–gold nanoparticle nanocomposites for SERS applications. *Analyst* **2015**, *140*, (16), 5640-5649.
4. Carpenter, A. W.; de Lannoy, C.-F.; Wiesner, M. R., Cellulose nanomaterials in water treatment technologies. *Environmental science & technology* **2015**, *49*, (9), 5277-5287.
5. Ye, S.; Jiang, L.; Wu, J.; Su, C.; Huang, C.; Liu, X.; Shao, W., Flexible amoxicillin-grafted bacterial cellulose sponges for wound dressing: in vitro and in vivo evaluation. *ACS applied materials & interfaces* **2018**, *10*, (6), 5862-5870.
6. Fernandes, S. C.; Sadocco, P.; Alonso-Varona, A.; Palomares, T.; Eceiza, A.; Silvestre, A. J.; Mondragon, I. a.; Freire, C. S., Bioinspired antimicrobial and biocompatible bacterial cellulose membranes obtained by surface functionalization with aminoalkyl groups. *ACS applied materials & interfaces* **2013**, *5*, (8), 3290-3297.
7. Chen, X.; Xu, X.; Li, W.; Sun, B.; Yan, J.; Chen, C.; Liu, J.; Qian, J.; Sun, D., Effective drug carrier based on polyethylenimine-functionalized bacterial cellulose with controllable release properties. *ACS Applied Bio Materials* **2018**, *1*, (1), 42-50.
8. Echeverry - Rendon, M.; Reece, L. M.; Pastrana, F.; Arias, S. L.; Shetty, A. R.; Pavón, J. J.; Allain, J. P., Bacterial Nanocellulose Magnetically Functionalized for Neuro - Endovascular Treatment. *Macromolecular bioscience* **2017**, *17*, (6), 1600382.
9. Guo, J.; Filpponen, I.; Johansson, L.-S.; Mohammadi, P.; Latikka, M.; Linder, M. B.; Ras, R. H.; Rojas, O. J., Complexes of magnetic nanoparticles with cellulose nanocrystals as regenerable, highly efficient, and selective platform for protein separation. *Biomacromolecules* **2017**, *18*, (3), 898-905.
10. Luo, X.; Lei, X.; Cai, N.; Xie, X.; Xue, Y.; Yu, F., Removal of heavy metal ions from water by magnetic cellulose-based beads with embedded chemically modified magnetite nanoparticles and activated carbon. *ACS Sustainable Chemistry & Engineering* **2016**, *4*, (7), 3960-3969.
11. Laurent, S.; Forge, D.; Port, M.; Roch, A.; Robic, C.; Vander Elst, L.; Muller, R. N., Magnetic iron oxide nanoparticles: synthesis, stabilization, vectorization, physicochemical characterizations, and biological applications. *Chemical reviews* **2008**, *108*, (6), 2064-2110.
12. Teja, A. S.; Koh, P.-Y., Synthesis, properties, and applications of magnetic iron oxide nanoparticles. *Progress in crystal growth and characterization of materials* **2009**, *55*, (1-2), 22-45.

13. Park, M.; Chang, H.; Jeong, D. H.; Hyun, J., Spatial deformation of nanocellulose hydrogel enhances SERS. *BioChip Journal* **2013**, *7*, (3), 234-241.
14. Petryayeva, E.; Krull, U. J., Localized surface plasmon resonance: Nanostructures, bioassays and biosensing—A review. *Analytica chimica acta* **2011**, *706*, (1), 8-24.
15. Champion, A.; Kambhampati, P., Surface-enhanced Raman scattering. *Chemical Society Reviews* **1998**, *27*, (4), 241-250.
16. Michaels, A. M.; Nirmal, M.; Brus, L., Surface enhanced Raman spectroscopy of individual rhodamine 6G molecules on large Ag nanocrystals. *Journal of the American Chemical Society* **1999**, *121*, (43), 9932-9939.
17. Carrabba, M. M.; Edmonds, R. B.; Rauh, R. D., Feasibility studies for the detection of organic surface and subsurface water contaminants by surface-enhanced Raman spectroscopy on silver electrodes. *Analytical chemistry* **1987**, *59*, (21), 2559-2563.
18. Wei, H.; Rodriguez, K.; Renneckar, S.; Vikesland, P. J., Environmental science and engineering applications of nanocellulose-based nanocomposites. *Environmental Science: Nano* **2014**, *1*, (4), 302-316.
19. Morales-Narváez, E.; Golmohammadi, H.; Naghdi, T.; Yousefi, H.; Kostiv, U.; Horak, D.; Pourreza, N.; Merkoçi, A., Nanopaper as an optical sensing platform. *ACS nano* **2015**, *9*, (7), 7296-7305.
20. Habibi, Y.; Goffin, A.-L.; Schiltz, N.; Duquesne, E.; Dubois, P.; Dufresne, A., Bionanocomposites based on poly (ϵ -caprolactone)-grafted cellulose nanocrystals by ring-opening polymerization. *Journal of Materials Chemistry* **2008**, *18*, (41), 5002-5010.
21. Bossa, N.; Carpenter, A. W.; Kumar, N.; de Lannoy, C.-F.; Wiesner, M., Cellulose nanocrystal zero-valent iron nanocomposites for groundwater remediation. *Environmental Science: Nano* **2017**, *4*, (6), 1294-1303.
22. Brinkmann, A.; Chen, M.; Couillard, M.; Jakubek, Z. J.; Leng, T.; Johnston, L. J., Correlating cellulose nanocrystal particle size and surface area. *Langmuir* **2016**, *32*, (24), 6105-6114.
23. Singhsa, P.; Narain, R.; Manuspiya, H., Bacterial cellulose nanocrystals (BCNC) preparation and characterization from three bacterial cellulose sources and development of functionalized BCNCs as nucleic acid delivery systems. *ACS Applied Nano Materials* **2017**, *1*, (1), 209-221.
24. George, J.; Kumar, R.; Sajeevkumar, V. A.; Ramana, K. V.; Rajamanickam, R.; Abhishek, V.; Nadanasabapathy, S., Hybrid HPMC nanocomposites containing bacterial cellulose nanocrystals and silver nanoparticles. *Carbohydrate polymers* **2014**, *105*, 285-292.
25. Chiang, I. C.; Chen, D. H., Synthesis of monodisperse FeAu nanoparticles with tunable magnetic and optical properties. *Advanced Functional Materials* **2007**, *17*, (8), 1311-1316.
26. Wang, J.; Wu, X.; Wang, C.; Rong, Z.; Ding, H.; Li, H.; Li, S.; Shao, N.; Dong, P.; Xiao, R., Facile synthesis of Au-coated magnetic nanoparticles and their application in bacteria detection via a SERS method. *ACS applied materials & interfaces* **2016**, *8*, (31), 19958-19967.

- 1
2
3 27. Saha, D.; Koga, K.; Takeo, H., Stable icosahedral nanoparticles in an as-grown Au–Fe
4 alloy. *The European Physical Journal D-Atomic, Molecular, Optical and Plasma Physics* **1999**,
5 *9*, (1), 539-542.
6
7 28. Lu, D.-l.; Domen, K.; Tanaka, K.-i., Electrodeposited Au– Fe, Au– Ni, and Au– Co Alloy
8 Nanoparticles from Aqueous Electrolytes. *Langmuir* **2002**, *18*, (8), 3226-3232.
9
10 29. Long, J.; Yi, H.; Li, H.; Lei, Z.; Yang, T., Reproducible ultrahigh SERS enhancement in
11 single deterministic hotspots using nanosphere-plane antennas under radially polarized excitation.
12 *Scientific reports* **2016**, *6*, 33218.
13
14 30. Qian, X.; Emory, S. R.; Nie, S., Anchoring molecular chromophores to colloidal gold
15 nanocrystals: surface-enhanced Raman evidence for strong electronic coupling and irreversible
16 structural locking. *Journal of the American Chemical Society* **2012**, *134*, (4), 2000-2003.
17
18 31. Vasconcelos, N. F.; Feitosa, J. P. A.; da Gama, F. M. P.; Morais, J. P. S.; Andrade, F. K.;
19 de Souza, M. d. S. M.; de Freitas Rosa, M., Bacterial cellulose nanocrystals produced under
20 different hydrolysis conditions: properties and morphological features. *Carbohydrate polymers*
21 **2017**, *155*, 425-431.
22
23 32. Roman, M.; Winter, W. T., Effect of sulfate groups from sulfuric acid hydrolysis on the
24 thermal degradation behavior of bacterial cellulose. *Biomacromolecules* **2004**, *5*, (5), 1671-1677.
25
26 33. Wu, X.; Lu, C.; Zhou, Z.; Yuan, G.; Xiong, R.; Zhang, X., Green synthesis and formation
27 mechanism of cellulose nanocrystal-supported gold nanoparticles with enhanced catalytic
28 performance. *Environmental Science: Nano* **2014**, *1*, (1), 71-79.
29
30 34. Rashid, M.; Gafur, M. A.; Sharafat, M. K.; Minami, H.; Miah, M. A. J.; Ahmad, H.,
31 Biocompatible microcrystalline cellulose particles from cotton wool and magnetization via a
32 simple in situ co-precipitation method. *Carbohydrate polymers* **2017**, *170*, 72-79.
33
34 35. He, F.; Zhao, D., Preparation and characterization of a new class of starch-stabilized
35 bimetallic nanoparticles for degradation of chlorinated hydrocarbons in water. *Environmental*
36 *science & technology* **2005**, *39*, (9), 3314-3320.
37
38 36. Lin, N.; Bruzzese, C. c.; Dufresne, A., TEMPO-oxidized nanocellulose participating as
39 crosslinking aid for alginate-based sponges. *ACS applied materials & interfaces* **2012**, *4*, (9), 4948-
40 4959.
41
42 37. Schwartzberg, A. M.; Grant, C. D.; Wolcott, A.; Talley, C. E.; Huser, T. R.; Bogomolni,
43 R.; Zhang, J. Z., Unique gold nanoparticle aggregates as a highly active surface-enhanced Raman
44 scattering substrate. *The Journal of Physical Chemistry B* **2004**, *108*, (50), 19191-19197.
45
46 38. Deckert - Gaudig, T.; Deckert, V., Ultraflat Transparent Gold Nanoplates—Ideal
47 Substrates for Tip - Enhanced Raman Scattering Experiments. *Small* **2009**, *5*, (4), 432-436.
48
49 39. Lin, K.-H.; Hu, D.; Sugimoto, T.; Chang, F.-C.; Kobayashi, M.; Enomae, T., An analysis
50 on the electrophoretic mobility of cellulose nanocrystals as thin cylinders: relaxation and end effect.
51 *RSC Advances* **2019**, *9*, (58), 34032-34038.
52
53 40. Semenikhin, N. S.; Kadasala, N. R.; Moon, R. J.; Perry, J. W.; Sandhage, K. H.,
54 Individually dispersed gold nanoshell-bearing cellulose nanocrystals with tailorable plasmon
55 resonance. *Langmuir* **2018**, *34*, (15), 4427-4436.
56
57
58
59
60

- 1
2
3 41. Csapó, E.; Sebők, D.; Makrai Babić, J.; Šupljika, F.; Bohus, G.; Dékány, I.; Kallay, N.;
4 Preočanin, T., Surface and structural properties of gold nanoparticles and their biofunctionalized
5 derivatives in aqueous electrolytes solution. *Journal of dispersion science and technology* **2014**,
6 35, (6), 815-825.
7
8 42. Lueck, H. B.; Daniel, D. C.; McHale, J. L., Resonance Raman study of solvent effects on
9 a series of triarylmethane dyes. *Journal of Raman spectroscopy* **1993**, 24, (6), 363-370.
10
11 43. Li, M.; Zhang, J.; Suri, S.; Sooter, L. J.; Ma, D.; Wu, N., Detection of adenosine
12 triphosphate with an aptamer biosensor based on surface-enhanced Raman scattering. *Analytical*
13 *chemistry* **2012**, 84, (6), 2837-2842.
14
15 44. Wei, H.; Leng, W.; Song, J.; Willner, M. R.; Marr, L. C.; Zhou, W.; Vikesland, P. J.,
16 Improved quantitative SERS enabled by surface plasmon enhanced elastic light scattering.
17 *Analytical chemistry* **2018**, 90, (5), 3227-3237.
18
19 45. Wei, H.; Huang, Q.; Vikesland, P. J., The Aromatic Amine p K_a Determines the Affinity
20 for Citrate-Coated Gold Nanoparticles: In Situ Observation via Hot Spot-Normalized Surface-
21 Enhanced Raman Spectroscopy. *Environmental Science & Technology Letters* **2019**, 6, (4), 199-
22 204.
23
24 46. Wei, H.; Leng, W.; Song, J.; Liu, C.; Willner, M. R.; Huang, Q.; Zhou, W.; Vikesland, P.
25 J., Real-time monitoring of ligand exchange kinetics on gold nanoparticle surfaces enabled by hot
26 spot-normalized surface-enhanced Raman scattering. *Environmental science & technology* **2018**,
27 53, (2), 575-585.
28
29 47. Wei, H.; McCarthy, A.; Song, J.; Zhou, W.; Vikesland, P. J., Quantitative SERS by hot
30 spot normalization–surface enhanced Rayleigh band intensity as an alternative evaluation
31 parameter for SERS substrate performance. *Faraday discussions* **2017**, 205, 491-504.
32
33 48. Dinish, U.; Balasundaram, G.; Chang, Y. T.; Olivo, M., Sensitive multiplex detection of
34 serological liver cancer biomarkers using SERS - active photonic crystal fiber probe. *Journal of*
35 *biophotonics* **2014**, 7, (11 - 12), 956-965.
36
37 49. Kowalska, A. A.; Kaminska, A.; Adamkiewicz, W.; Witkowska, E.; Tkacz, M., Novel
38 highly sensitive Cu - based SERS platforms for biosensing applications. *Journal of Raman*
39 *spectroscopy* **2015**, 46, (5), 428-433.
40
41 50. Wu, Z.; Liu, Y.; Zhou, X.; Shen, A.; Hu, J., A “turn-off” SERS-based detection platform
42 for ultrasensitive detection of thrombin based on enzymatic assays. *Biosensors and Bioelectronics*
43 **2013**, 44, 10-15.
44
45 51. Bao, Z. Y.; Liu, X.; Chen, Y.; Wu, Y.; Chan, H. L.; Dai, J.; Lei, D. Y., Quantitative SERS
46 detection of low-concentration aromatic polychlorinated biphenyl-77 and 2, 4, 6-trinitrotoluene.
47 *Journal of hazardous materials* **2014**, 280, 706-712.
48
49 52. Yang, S.; Dai, X.; Stogin, B. B.; Wong, T.-S., Ultrasensitive surface-enhanced Raman
50 scattering detection in common fluids. *Proceedings of the National Academy of Sciences* **2016**,
51 113, (2), 268-273.
52
53 53. Shrivastava, A.; Gupta, V. B., Methods for the determination of limit of detection and limit
54 of quantitation of the analytical methods. *Chronicles of young scientists* **2011**, 2, (1), 21.
55
56
57
58
59
60

1
2
3 54. Robinson, I.; Tung, L. D.; Maenosono, S.; Wälti, C.; Thanh, N. T., Synthesis of core-shell
4 gold coated magnetic nanoparticles and their interaction with thiolated DNA. *Nanoscale* **2010**, *2*,
5 (12), 2624-2630.
6
7
8
9
10
11
12

13 **Graphical abstract**

